Metal Embedded Optical Fiber Sensors: Laser-Based Layered Manufacturing Procedures

Hamidreza Alemohammad
e-mail: hamidreza.alemohammad@uwaterloo.ca

Ehsan Toyserkani

Department of Mechanical and Mechatronics
Engineering,
University of Waterloo,
Waterloo, ON N2L 3G1, Canada

This paper describes laser-based layered manufacturing processes for embedding optical fiber Bragg gratings (FBGs) in metal structures to develop cutting tools with embedded sensors. FBG is a type of optical fiber that is used for the measurement of parameters manifesting as the changes of strain or temperature. The unique features of FBGs have encouraged their widespread use in structural measurements, failure diagnostics, thermal measurements, pressure monitoring, etc. Considering the unique features of FBGs, embedding of the sensors in metal parts for in-situ load monitoring is a cutting-edge research topic with a variety of applications in machining tools, aerospace, and automotive industries. The metal embedding process is a challenging task, as the thermal decay of UV-written gratings can start at a temperature of $\sim 200\,^\circ C$ and accelerates at higher temperatures. The embedding process described in this paper consists of low temperature laser microdeposition of on-fiber silver thin films followed by nickel electroplating in a steel part. A microscale laser-based direct write (DW) method, called laser-assisted maskless microdeposition (LAMM), is employed to deposit silver thin films on optical fibers. To attain thin films with optimum quality, a characterization scheme is designed to study the geometrical, mechanical, and microstructural properties of the thin films in terms of the LAMM process parameters. To realize the application of embedded FBG sensors in machining tools, the electroplating process is followed by the deposition of a layer of tungsten carbide-cobalt (WC-Co) by using laser solid freeform fabrication (LSFF). An optomechanical model is also developed to predict the optical response of the embedded FBGs. The performance of the embedded sensor is evaluated in a thermal cycle. The results show that the sensor attains its linear behavior after embedding. Microscopic analysis of the tool with the embedded sensor clearly exhibits the integrity of the deposited layers without cracks, porosity, and delamination. [DOI: 10.1115/1.4004203]

Keywords: optical fiber sensors, embedded sensors, on-fiber thin films, laser-based layered manufacturing, structural monitoring

Introduction

FBGs are periodic modulations of the index of refraction in the core of single-mode optical fibers [1]. Optical fibers are made of fused silica, and the gratings are inscribed in the core using UV or femtosecond laser radiation [2]. The grating causes the reflection of the input light spectrum at a specific wavelength, called Bragg wavelength, with a narrow bandwidth. Due to photo-elastic and thermo-optic effects, the reflection spectrum of FBGs is sensitive to strain and temperature. As a result, any parameter that manifests as the changes of temperature or strain can be measured with this type of sensor [2]. The distinctive features of FBGs encourage the development of embedded sensors in metal parts for in-situ load measurements, structural health monitoring, and failure diagnostics. Promising applications can be sought for FBGs in various industrial sectors including, but not limited to, aerospace, petroleum, and automotive industries. For instance, embedded FBG sensors in machining tools enable in-situ monitoring of structural and thermal loads applied to the tools during the manufacturing process, which can boost the productivity and performance. Compared with conventional electric and electromagnetic sensing devices such as MEMS pressure and temperature sensors, optical fiber sensors are significantly advantageous. They are known for their light weight, small size (125 μm diameter), long-term durability, and long-range linearity. Moreover, they are robust to external electromagnetic noise and

disturbance and are corrosion-resistant. In addition, arrays of FBG sensors can be produced on a single strand of optical fiber to capture the measurement data at multiple points. As a result, masses of wires which are typically observed in thin film transducers are not required. When it comes to remote sensing, optical fibers can transfer data at long distances with very low losses as opposed to electrical sensors, which are prone to Ohmic losses. The attenuation of standard single-mode optical fibers (Corning SMF-28) used for telecommunication applications is less than 0.22 db/km [3].

For structural health monitoring and failure diagnostics, surface mounted or embedded FBG sensors can replace strain gauges. According to the literature, several methods have been proposed to embed FBGs in composite materials, concrete, and metals [4–7]. Compared with electrical and electromagnetic sensors, such as thin film thermocouples, strain gauges, and MEMS transducers, optical fibers are electrically insulated. As a result, metal-embedding process does not require the inclusion of insulators [8,9].

Despite the widespread use of optical fiber sensors in structural health monitoring, embedding of optical fibers in metallic structures is a challenging task. The challenge arises from the sensitivity of FBGs to high temperatures. The UV-written grating in FBG can start to degrade at a temperature of $\sim 200\,^\circ C$ and the decay speed increases with temperature [2,10]. In addition, the optical fiber can structurally been damaged at very high temperatures. The glass transition temperature for fused silica is $\sim 1200\,^\circ C$ [11]. As a result, any embedding process that directly employs molten metal can cause permanent failure in optical fibers.

The literature shows that research in the area of metal-embedded optical fiber sensors is growing. Lee et al. studied the performance of

fiber optic Fabry–Perots embedded in aluminum by casting in graphite molds [12]. Li et al. investigated the process of embedding FBGs in nickel and steel using electrodeposition and shape deposition manufacturing. FBGs are sputtered with a 1 μm thick layer of titanium followed by 2 μm Ni sputtering. The process continues by nickel electroplating in nickel sulfamate bath. The results show that the sensor retains its linear behavior and its thermal sensitivity is increased from 10 to 21 pm/°C [7]. Sandlin et al. proposed a method of coating FBGs with electroplating and brazing [13]. For embedding FBG sensors, low temperature electroplating is superior to casting, as the formation of residual stress is minimal. Another low temperature method proposed in the literature for embedding optical fibers is ultrasonic consolidation, which has been used for embedding optical fibers in aluminum. Experimental results in [14] shows the success of this embedding process by illuminating the optical fibers from one end and observing the light passing through and detected at the other end of the optical fibers.

The electroplating process for embedding FBGs in metals requires thin films of conductive materials predeposited on optical fibers. Various methods have been proposed for the deposition of the on-fiber thin films. Lupi et al. coated FBGs with zinc and copper. They used electrowinning for the deposition of the metallic layer after precoating the fiber with aluminum [15]. Li et al. have employed magnetron sputtering for titanium and nickel deposition on FBGs. According to the literature, electrowinning, sputtering, electron beam evaporation, and electroplating techniques are methods that have been employed for the deposition of on-fiber titanium, silver, gold, platinum, zinc, lead, and copper films [15–19].

An alternative method of on-fiber thin film deposition is DW methods. To the best knowledge of the authors, in spite of their advantages, the DW methods have not been employed for on-fiber thin film deposition. Compared with the bulk deposition methods, DW methods are far more flexible in terms of material selection and maskless deposition. The deposition is typically performed at low temperatures, which widen the window of materials that can be used as substrate. In addition, the DW methods do not require temperature/pressure controlled chambers. All these features make the DW methods fast and inexpensive for thin film deposition. Although, the conventional methods such as sputtering are efficient for the deposition of thin films with nanoscale feature sizes, the DW methods are mostly effective for larger sizes in the range of 10–100 μm. Despite different names for direct writing technologies, all of them share a common feature: selective and layer-by-layer deposition without the use of masks.

This paper addresses a new technology for embedding FBGs in metal cutting tools. In this paper, the embedding process including laser-based additive manufacturing in micro- and macro-scale and electroplating are elaborated and characterized. First, optical fibers are coated, prior to electroplating, with a thin film of silver by using direct printing and laser sintering of silver nanoparticles. The silver-coated optical fibers are then embedded in a steel substrate using nickel electroplating. To realize the application of embedded FBG sensors in machining tools, a hard machining surface, made of tungsten carbide-cobalt (WC-Co), is deposited by laser solid freeform fabrication (LSFF) on the steel part. The embedded FBG can act as a load and temperature monitoring device when the machining tool is in service. The embedding process has been introduced by the authors in a previous publication [20].

In addition to the fabrication procedures, an optomechanical model, consisting of the photo-elastic and thermo-optic properties of optical fibers coupled with the thermal-structural finite elements (FE) model of the metal part, is also developed. The experimental and modeling results are used for the analysis of the response of the embedded FBG.

Structural and OptoMechanical Modeling of Metallic Part and Embedded FBG Sensors

Governing Physics. FBG, with submicron periodic modulations of the index of refraction, functions primarily as a filter
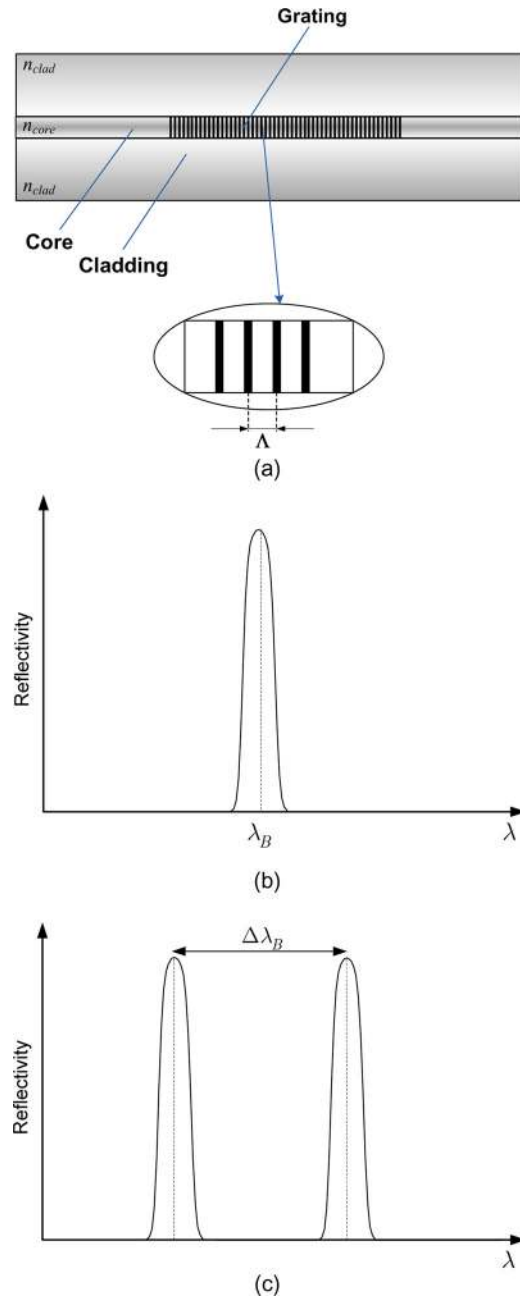
Fig. 1 (*a*) FBG with modulations of the index of refraction, (*b*) FBG reflection spectrum, and (*c*) Bragg wavelength shift resulted from changes in temperature and/or strain

(Fig. 1(*a*)). When a Bragg grating is exposed to a broadband spectrum of light, the guided light wave, propagating along the optical fiber, is scattered by each grating plane. As a result, parts of the spectrum at a specific wavelength, matching the Bragg condition (Eq. (1)), are reflected back. The coupling between the forward and backward propagating modes results in a resonance condition. The resonance occurs at a specific wavelength called the Bragg wavelength (λ_B) with the maximum reflectivity. Wavelengths which are not coincident with the Bragg condition degenerate progressively with weak reflections, whereas wavelengths close to the resonance wavelength determined by the Bragg condition (Eq. (1)) undergo strong reflections. Figure 1(*b*) shows the reflection spectrum of a uniform Bragg grating. The Bragg wavelength is related to the effective propagating mode index of refraction (n_{eff}) and the grating period (Λ), as defined in the Bragg condition [2,21]

$$\lambda_B = 2n_{\mathrm{eff}}\Lambda \qquad (1)$$

n_{eff} is defined in terms of the light wave propagation constant obtained by solving the light wave equation in the optical fiber [22].

The index of refraction in dielectric materials such as silica changes with strain and temperature due to photo-elastic and thermo-optic effects. As a result, the reflection spectrum of FBGs changes by applying structural loading or temperature. The photo-elastic and thermo-optic effects are described as [23–25]

$$
\begin{aligned}
\Delta n_1 = & -\frac{n_1^3}{2}(p_{11}e_1 + p_{12}(e_2 + e_3)) + \left(\frac{\partial n}{\partial T}\right)\Delta T \\
& + \frac{n_1^3}{2}(p_{11} + 2p_{12})\alpha\Delta T \\
\Delta n_2 = & -\frac{n_2^3}{2}(p_{11}e_2 + p_{12}(e_1 + e_3)) + \left(\frac{\partial n}{\partial T}\right)\Delta T \\
& + \frac{n_2^3}{2}(p_{11} + 2p_{12})\alpha\Delta T \\
\Delta n_3 = & -\frac{n_3^3}{2}(p_{11}e_3 + p_{12}(e_1 + e_2)) + \left(\frac{\partial n}{\partial T}\right)\Delta T \\
& + \frac{n_3^3}{2}(p_{11} + 2p_{12})\alpha\Delta T \\
\Delta n_4 = & -n_4^3\frac{(p_{11} - p_{12})}{4}e_4 \\
\Delta n_5 = & -n_5^3\frac{(p_{11} - p_{12})}{4}e_5 \\
\Delta n_6 = & -n_6^3\frac{(p_{11} - p_{12})}{4}e_6
\end{aligned}
\tag{2}
$$

where n_i's ($i = 1, ..., 6$) are the elements of the index of refraction tensor, e_i's ($i = 1, ..., 6$) are the elements of the strain tensor, and p_{ij}'s ($i, j = 1, 2$) are the component of strain-optic tensor, called Pockel's photo-elastic constant, and $\frac{\partial n}{\partial T}$ is a constant showing the thermal sensitivity of the index of refraction. ΔT denotes temperature variation, and α is the coefficient of thermal expansion. The optomechanical properties of standard optical fibers are listed in Table 1.

The grating period (Λ) is also affected by temperature and strain causing further changes in the reflection spectrum. Assuming that e_1 is aligned with the optical fiber axis, as shown in Fig. 2

$$
\Delta\Lambda = e_1\Lambda \tag{3}
$$

When FBG is under uniform strain and temperature distributions, a shift in the Bragg wavelength occurs (Fig. 1(c)). The change in the Bragg wavelength ($\Delta\lambda_B$), in terms of the variations of n_{eff} and Λ under uniform elongation (Δl) and temperature variation (ΔT), is expressed as [21]

$$
\Delta\lambda_B = 2\left(\Lambda\frac{\partial n_{\text{eff}}}{\partial l} + n_{\text{eff}}\frac{\partial\Lambda}{\partial l}\right)\Delta l + 2\left(\Lambda\frac{\partial n_{\text{eff}}}{\partial T} + n_{\text{eff}}\frac{\partial\Lambda}{\partial T}\right)\Delta T \tag{4}
$$

In FBGs, the gratings are inscribed in single-mode optical fibers, which are weakly guided ($n_{\text{clad}} \approx n_{\text{core}}$). For guided modes, the effective mode index of refraction (n_{eff}) satisfies $n_{\text{clad}} < n_{\text{eff}} < n_{\text{core}}$. Therefore, the modified effective mode index of refraction for the optical fiber exposed to strain components or temperature variations can be approximated as $n_{\text{eff}} \approx n_2$ or $n_{\text{eff}} \approx n_3$,

Table 1 Optomechanical properties of optical fibers

Parameter	Value
α (°C^{-1})	0.55×10^{-6}
p_{11}	0.113
p_{12}	0.252
$\partial n/\partial T$ (RIU/°C)	1.2×10^{-5}
n_{eff}	1.44405
Λ (nm)	537
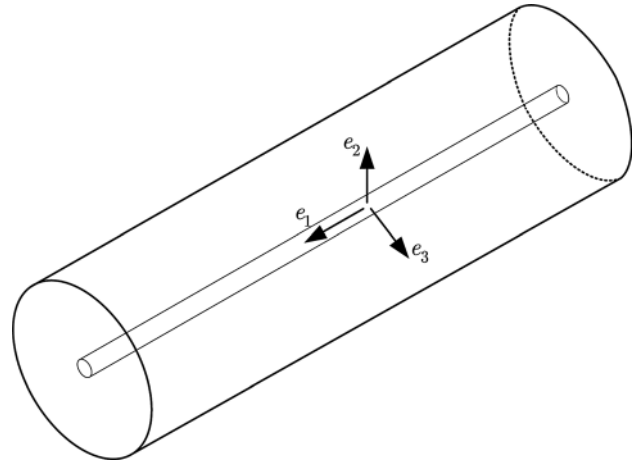
Fig. 2 Strain components e_1, e_2, and e_3 applied on optical fiber

where n_2 and n_3 are the transverse components of the index of refraction in the optical fiber. If $e_2 \neq e_3$, there exist two orthogonal guided modes with two effective indices of refraction (n_{eff_1} and n_{eff_2}). By substituting n_2 and n_3 with n_{eff_1} and n_{eff_2} in Eq. (2), the changes in the effective modes index of refraction are given by

$$
\begin{aligned}
\Delta n_{\text{eff}_1} = & -\frac{n_{\text{eff}_1}^3}{2}(p_{11}e_2 + p_{12}(e_1 + e_3)) + \left(\frac{\partial n}{\partial T}\right)\Delta T \\
& + \frac{n_{\text{eff}_1}^3}{2}(p_{11} + 2p_{12})\alpha\Delta T \\
\Delta n_{\text{eff}_2} = & -\frac{n_{\text{eff}_2}^3}{2}(p_{11}e_3 + p_{12}(e_1 + e_2)) + \left(\frac{\partial n}{\partial T}\right)\Delta T \\
& + \frac{n_{\text{eff}_2}^3}{2}(p_{11} + 2p_{12})\alpha\Delta T
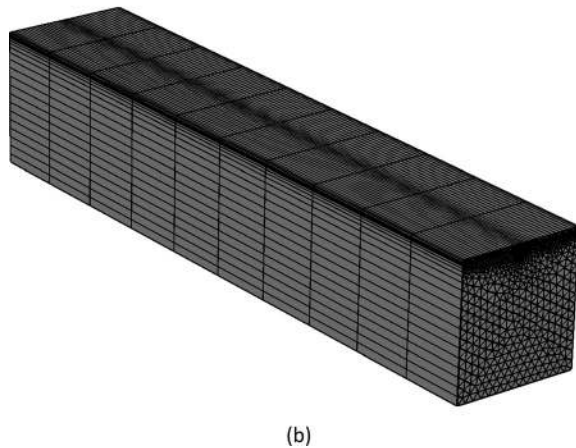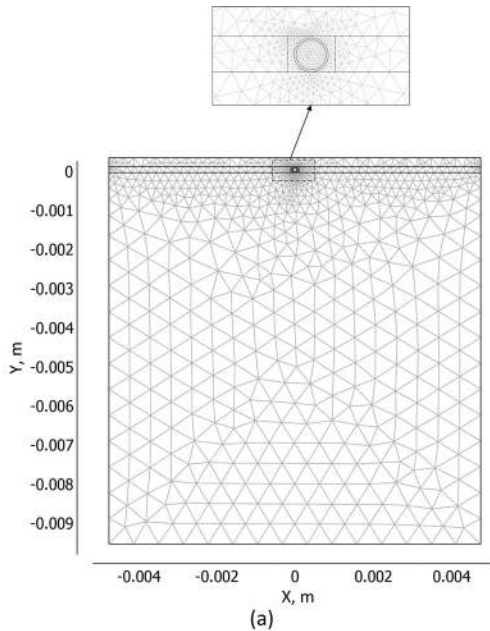\end{aligned}
\tag{5}
$$

Equation (4) can be rewritten as

$$
\Delta\lambda_B = 2(\Lambda\Delta n_{\text{eff}} + n_{\text{eff}}\Delta\Lambda)_{\Delta T=0} + 2(\Lambda\Delta n_{\text{eff}} + n_{\text{eff}}\Delta\Lambda)_{\Delta l=0} \tag{6}
$$

where $\Delta\Lambda = e_1\Lambda$ and $e_1 = e_2 = e_3 = \alpha\Delta T$ when $\Delta l = 0$. By substituting Eqs. (3) and (5) in Eq. (6)

$$
\begin{aligned}
\frac{\Delta\lambda_{B_1}}{\lambda_B} = & e_1 - \frac{n_{\text{eff}_1}^2}{2}(p_{12}e_1 + p_{11}e_2 + p_{12}e_3) + \frac{1}{n_{\text{eff}_1}}\left(\frac{\partial n}{\partial T}\right)\Delta T \\
& + \frac{n_{\text{eff}_1}^2}{2}(p_{11} + 2p_{12})\alpha\Delta T \\
\frac{\Delta\lambda_{B_2}}{\lambda_B} = & e_1 - \frac{n_{\text{eff}_2}^2}{2}(p_{12}e_1 + p_{12}e_2 + p_{11}e_3) + \frac{1}{n_{\text{eff}_2}}\left(\frac{\partial n}{\partial T}\right)\Delta T \\
& + \frac{n_{\text{eff}_2}^2}{2}(p_{11} + 2p_{12})\alpha\Delta T
\end{aligned}
\tag{7}
$$

The splitting of the reflectivity spectrum of FBGs into two peaks with Bragg wavelengths λ_{B_1} and λ_{B_2} is called birefringence. Since it is caused by external loads, it is also known as stress induced birefringence. In cases where the difference between the transverse strain components is small, the individual peaks overlap; as a result, the birefringence may not be clearly identified in the reflection spectrum. In special cases, if the transverse components are equal ($e_2 = e_3$), there is no peak splitting and birefringence, and Eq. (7) is reduced to

$$
\begin{aligned}
\frac{\Delta\lambda_B}{\lambda_B} = & e_1 - \frac{n_{\text{eff}}^2}{2}[(p_{11} + p_{12})e_2 + p_{12}e_1] + \frac{1}{n_{\text{eff}}}\left(\frac{\partial n}{\partial T}\right)\Delta T \\
& + \frac{n_{\text{eff}}^2}{2}(p_{11} + 2p_{12})\alpha\Delta T
\end{aligned}
\tag{8}
$$

Fig. 3 Meshed model for thermal–structural finite element analysis in COMSOL multiphysics

Table 2 Material properties for thermal–structural finite element analysis

Parameter	Value
$E_{\text{fiber}}(\text{GPa})$	70
$E_{\text{steel}}(\text{GPa})$	200
$E_{\text{nickel}}(\text{GPa})$	219
$\alpha_{\text{fiber}}(^{\text{o}}\text{C}^{-1})$	0.55×10^{-6}
$\alpha_{\text{steel}}(^{\text{o}}\text{C}^{-1})$	12.3×10^{-6}
$\alpha_{\text{nickel}}(^{\text{o}}\text{C}^{-1})$	13.4×10^{-6}
ν_{fiber}	0.17
ν_{steel}	0.33
ν_{nickel}	0.31

In the FE analysis with COMSOL multiphysics, the GMRES linear solver with algebraic multigrid preconditioning and the quality of multigrid hierarchy of 5 was used.

The FE modeling is based on the elastic stress-strain-temperature relations

$$e_i = \frac{\nu_{ij}\sigma_j}{E} + \delta_i \alpha \Delta T \qquad i, j = 1, ..., 6 \qquad (9)$$

where σ_j and e_i are the elements of stress and strain tensors. E is the modulus of elasticity, and δ_i is defined as

$$\begin{aligned} \delta_i = 1 & \quad \text{for} \quad i = 1, 2, 3 \\ \delta_i = 0 & \quad \text{for} \quad i = 4, 5, 6 \end{aligned} \qquad (10)$$

ν_{ij}'s are the elements of $[\nu]$ defined as

$$[\nu] = \begin{bmatrix} 1 & -\nu & -\nu & 0 & 0 & 0 \\ -\nu & 1 & -\nu & 0 & 0 & 0 \\ -\nu & -\nu & 1 & 0 & 0 & 0 \\ 0 & 0 & 0 & 1+\nu & 0 & 0 \\ 0 & 0 & 0 & 0 & 1+\nu & 0 \\ 0 & 0 & 0 & 0 & 0 & 1+\nu \end{bmatrix} \qquad (11)$$

where ν is Poisson's ratio. It is assumed that the strain components are continuous at the interfaces.

The strain components obtained from structural analysis were used in the optomechanical model of FBGs to find the anisotropic indices of refraction and the modified effective mode index of refraction in the optical fiber from Eq. (5). Accordingly, the shift of the Bragg wavelength is obtained from Eq. (8).

Embedding/Fabrication Procedures

Fabrication of the metal part with embedded FBG sensors consists of a sequence of processes, as shown in Fig. 4. They are

(1) Deposition of on-fiber conductive thin film,
(2) Nickel electroplating,
(3) LSFF of desired materials. In this study, we investigated the application of the embedded FBG sensor in cutting tools; therefore, nickel electroplating is followed by the deposition of WC-Co using the LSFF process.

Laser Direct Fabrication of On-fiber Thin Films.

Laser-Assisted Maskless Microdeposition Process. Before electroplating, the optical fibers need to be coated by a conductive layer. In this study, we selected silver, which was deposited by LAMM on FBGs. The details of the process are available in Ref. [26].

LAMM is categorized as a laser direct write process. In LAMM, nanoparticles of silver suspended in a liquid are atomized pneumatically. The generated aerosol is carried to a deposition head by the flow of nitrogen gas. In the deposition head, the aerosol is aerodynamically focused by the flow of a secondary gas
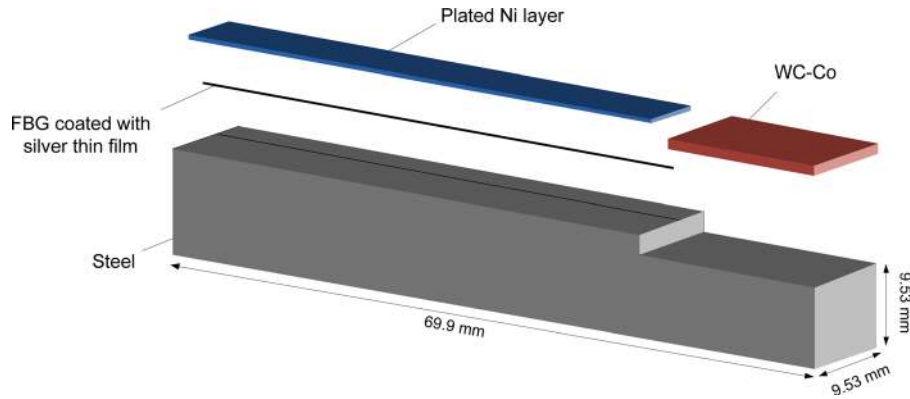
Structural Modeling of the Part with Embedded FBG Sensor. The sensitivity of the embedded FBG sensor depends on the geometrical features and the mechanical properties of the metallic structures. In order to study the sensitivity of the embedded FBG, a model has been developed. The model consists of

(1) A structural model to obtain the state of stress and strain distributions in the embedded FBG,
(2) An optomechanical model to obtain the spectral response of the embedded FBG.

To find the state of stress and strain in the embedded optical fiber, a 3D structural–thermal FE model was developed in COMSOL multiphysics. The meshed model is shown in Fig. 3. The 3D model was constructed by extruding the cross section meshed with triangular elements. As shown, the fiber coated with a thin layer of silver is embedded in a groove made in the steel part, and the top layer is electroplated nickel. The mechanical properties of the materials used in the FE modeling are listed in Table 2.

After the mesh independency analysis, the cross section of the part was discretized with 2106 triangular mesh elements, which were extruded to form the 3D part. As seen, finer mesh sizes were chosen at the location of the optical fiber and the electroplated nickel layer.

Fig. 4 Schematic diagram of the fabrication processes for embedding FBG sensor

stream called sheath gas. The focused aerosol stream with a diameter of 15–20 μm is ejected from the deposition head and reaches a moving substrate. After the deposition, a laser beam is directed for post-annealing and sintering of the as-deposited material. The process parameters involved in LAMM are listed in Table 3.

The LAMM process is superior to the conventional thin film deposition technologies such as physical vapor deposition methods in different aspects. LAMM is a maskless and direct write process, which eliminates the addition and removal of materials. This can reduce the production time and cost significantly. Thicknesses in the range of 500 nm to tens of micrometers can be controlled by the layer-by-layer deposition fashion. The process can be performed at atmospheric pressure and does not need clean room facilities. Compared with other direct write methods such as inkjet printing, laser-induced forward transfer (LIFT), and matrix-assisted pulsed-laser evaporation direct write (MAPLE DW) [27] the gap between the deposition head and the substrate can vary from 2 to 5 mm, which enables conformal pattern deposition on nonplanar surfaces such as optical fibers. The metal thin film formation using LAMM is performed in two steps as opposed to LIFT and MAPLE DW methods [27]. In LAMM, the aerosol of metal nanoparticles is first deposited and then sintered using the laser beam to form solid coatings, whereas, in LIFT and MAPLE DW methods, the laser beam is used for the ablation of the material from the target support.

The silver nanoparticles need to be sintered by applying heat after the deposition. For this purpose, the substrate with the deposited patterns can be heated in a furnace or on a hot plate. However, the laser spot heating provides a faster sintering process by creating a local heating zone and preventing the entire substrate from being exposed to high temperatures.

The laser sintering mechanism of nanoparticles is shown in Fig. 5. When the nanoparticle solution is radiated by the laser beam, the solvent evaporates and the particles agglomerate to form solid structures. As shown in Fig. 5, the agglomerated particles produce "neck-shape" structures [28–30]. Agglomeration, which leads to the reduction of surface energy, occurs as a result of the atomic diffusion between the nanoparticles. Different diffusion mechanisms can occur in the laser sintering process: surface diffusion, grain boundary diffusion, and lattice diffusion. In the laser sintering

of nanoparticles, the dominance of a diffusion mechanism depends on the size of nanoparticles. In the early stages of the sintering process, surface diffusion and grain boundary diffusion, with lower activation energies than lattice diffusion, are dominant. The laser sintering of nanoparticle solution involves liquid evaporation and densification resulting in an increased electrical conductivity [31]. As a result, weight loss and the formation of residual stress are prevalent in this process.

Path Planning for LAMM. During the deposition process, the FBG was mounted on a rotational stage and fixed and pulled at the ends to keep it straight beneath the deposition head. The films were deposited on the optical fiber by moving it in a programmed path relative to the deposition head. To coat a desired length of the fiber, the silver tracks were deposited adjacent to each other with spacing of 20–25 μm. Figure 6 shows the relative path followed by the deposition head.

During the deposition process, only one side of the optical fiber was exposed to the aerosol of silver nanoparticles. To achieve a uniform coating thickness, the optical fiber was rotated by 90° in each round of deposition, as displayed in Fig. 7.
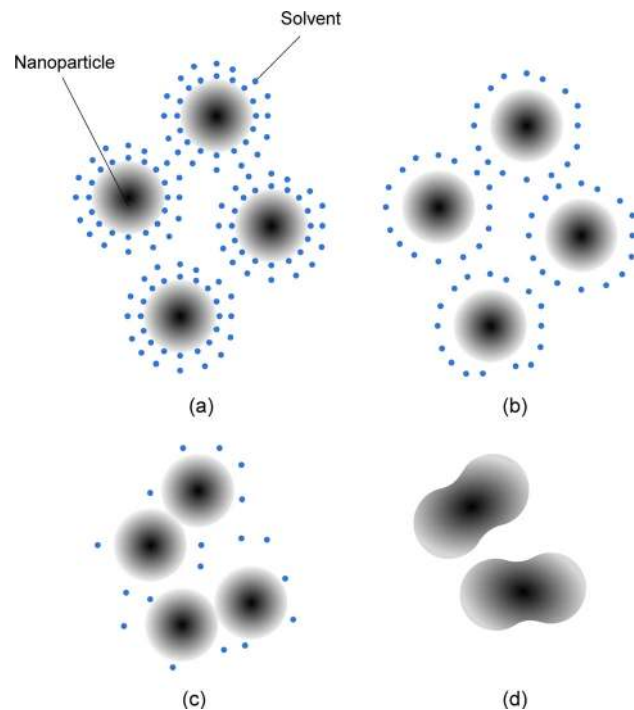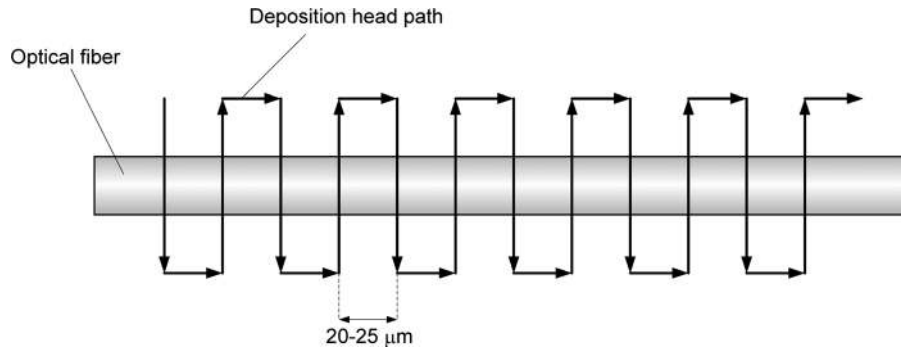

Table 3 LAMM process parameters

Deposition process parameters	Laser sintering process parameters
Atomizer gas flow rate (cm^3/min)	Laser power (W)
Sheath gas flow rate (cm^3/min)	Laser scanning speed (mm/s)
Virtual impactor gas flow rate (cm^3/min)	Focused laser beam diameter (μm)
Deposition speed (mm/s)	—
Deposition tip diameter (μm)	—

Fig. 5 Laser sintering mechanism of nanoparticles (*a*) before sintering, (*b*) liquid evaporation, (*c*) start of agglomeration, and (*d*) end of agglomeration

Fig. 6 Path followed by the deposition head of LAMM relative to the optical fiber for the deposition of on-fiber silver thin films
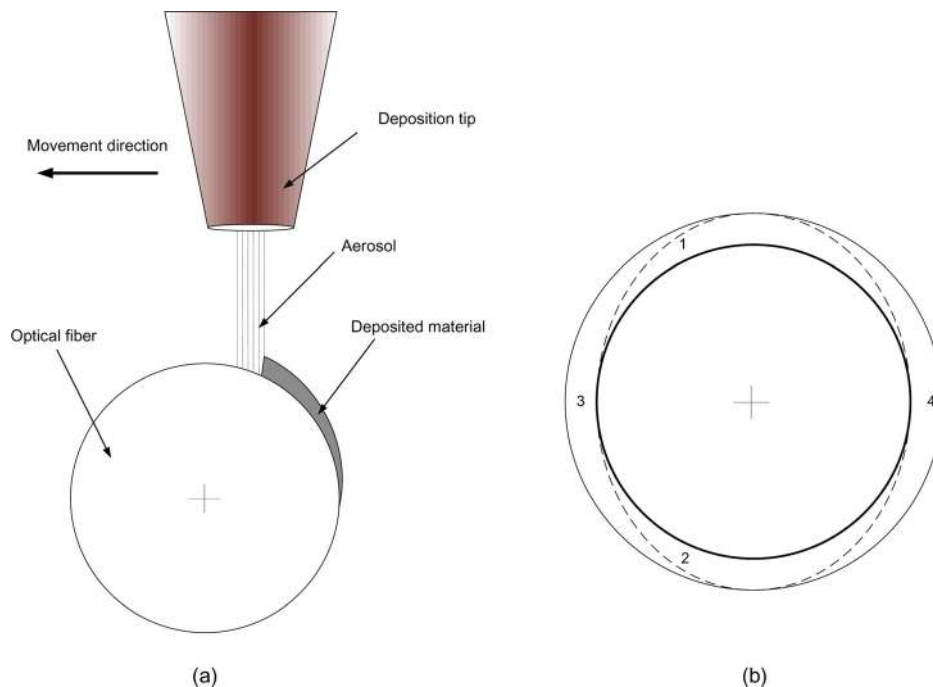
LAMM Process Characterization and Optimization. As listed in Table 3, the LAMM process involves various parameters that can be categorized into two classes: deposition and laser sintering parameters. In the LAMM process, the deposition parameters primarily affect the geometrical features such as the thickness and the width of the films. The microstructural and mechanical properties are mostly affected by the laser processing parameters [26]. The optimum parameters were obtained for planar substrates and further tuned for the deposition on the nonplanar surface of optical fibers, based on our previous study [25].

Materials and Experimental Procedures for Characterizing LAMM. Silver was selected as the coating material for FBGs. Among the materials that are available as nanoink, silver has good adhesion to silica. Silver nanoparticles suspended in ethylene glycol ($C_2H_4(OH)_2$) were used in the experiments. The suspension, supplied by Nanosize Ltd., contained 50 wt. % of silver nanoparticles with an average particle size of 50 nm.

An FBG with a Bragg wavelength of 1550 nm and grating length of 14 mm (O/E LAND Inc., Quebec, QC, Canada) was selected. The as-received FBG was coated with a polymeric layer to protect it during shipping and handling. The polymer coating was chemically stripped by immersing the fiber in acetone for about 15 min.

Before the thin film deposition on the optical fiber, the LAMM process was characterized. The deposition, followed by laser sintering, was performed on planar silica (SiO_2) substrates at different process parameters. The laser power at the process zone was measured by a power meter (L30A Thermal Head, OPHIR, Logan, UT, USA). After the deposition and laser sintering, the samples were examined by scanning electron microscope (SEM) to study the microstructure of the deposited tracks. A LEO 1530 field emission scanning electron microscope was used for this purpose. The crystalline structure of the thin films was examined with x-ray Diffraction (XRD) by using a micro X-ray diffraction machine with Cu-K$_\alpha$ radiation. To obtain the effect of laser parameters on the mechanical properties of the deposited thin films, nano-indentation tests using Hysitron TI 900 TriboIndenter (Hysitron, Inc., Minneapolis, MN) were performed.

Samples with different laser sintering parameters were made. The optimized process parameters resulting in fine edge deposition tracks were identified for the deposition with pneumatic atomizer as listed in Table 4 [23]. The samples were fabricated with different laser powers at a laser speed of 0.25 mm/s. Laser powers of 1.35 W, 2.41 W, and 3.28 W at the process zone with a beam diameter of 200 μm were used in the experiments.


Fig. 7 (*a*) Schematic diagram of the LAMM deposition tip and the optical fiber and (*b*) for each set of depositions the fiber is rotated by 90°

Table 4 LAMM process parameters for the process characterization and the deposition of silver thin films on optical fibers

Parameter	Value
Atomizer flow rate (cm^3/min)	740–750
Sheath gas flow rate (cm^3/min)	100
Virtual impactor gas flow rate (cm^3/min)	700
Deposition tip diameter (μm)	200
Deposition velocity (mm/s)	3
Laser power at the process zone (W)	1.35,2.41,3.28[a]
Laser scanning speed (mm/s)	0.25
Laser beam diameter (μm)	200

[a]Laser power used for the sintering of on-fiber silver thin films
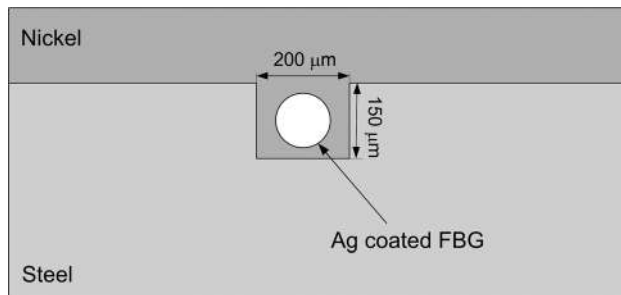
Fig. 8 Schematic cross section of the sample with embedded FBG

Nickel Electroplating for Embedding FBGs. The on-fiber thin-film deposition process was followed by nickel electroplating in a steel part. The electroplating was used for embedding due to its low temperature and formation of no or very low amount of residual stress [7]. The rational for using nickel is that its mechanical properties (Young's modulus and coefficient of thermal expansion) are close to those of steel, and it can be easily electroplated on steel. Figure 8 shows the schematic cross section of the sample with embedded FBG. A microgroove with a depth of 150 μm and a width of 200 μm was fabricated on a block of steel. The silver-coated optical fiber was placed in and aligned with the groove. Afterward, the sample was transferred to the nickel electroplating bath. A nickel sulfamate bath was used for the electrodeposition. Before plating, the recipient surfaces were polished, and the surfaces that did not need nickel plating were covered by Kapton tape. Prior to plating in the sulfamate bath, the sample was placed in steel activator bath in which a current density of 0.215 mA/mm^2 with reverse polarity was applied for 2–3 min. It was followed by a forward current density of 0.215 mA/mm^2 for 2 min. Then, the sample was rinsed with distilled water, dried, and placed in the nickel sulfamate bath. A current density of 0.215 mA/mm^2 was applied for about 14–16 h, resulting in a plated nickel layer with a thickness of 230 μm. The chemical compositions of the electroplating baths are given in Table 5.

Table 5 Chemical composition of sulfamate and steel activator baths for nickel electroplating

Sulfamate Bath	
Nickel Sulfamate, Ni (SO$_3$NH$_2$)$_2$	300–450 g/l
Nickel Chloride, NiCl$_2$.6H$_2$O	0–30 g/l
Boric Acid, H$_3$BO$_3$	30–45 g/l
Steel Activator Bath	
Nickel chloride hexahydrate	60 g/l
Hydrochloric acid	125 ml/l

Table 6 LSFF process parameters for the deposition of WC-Co using CW Ytterbium fiber laser

Parameter	Value
Laser power (W)	400
Laser beam wavelength (nm)	1064
Laser scanning speed (mm/s)	6
Powder feed rate (g/min)	8
Laser beam diameter (mm)	1.5

LSFF of WC-Co. To realize the application of the embedded FBG sensors for structural monitoring of cutting tools, a layer of WC-Co was deposited on the steel part in the proximity of the nickel plated layer using the LSFF process equipped with the 1 kW CW Ytterbium fiber laser. The details of the LSFF process characterization for the deposition of WC-Co are available in the previous publications of the authors [32]. The LSFF processing parameters are listed in Table 6.

The sample made by this fabrication protocol has a core of steel with embedded FBG sensors and a hard material on the surface used for machining. WC-Co is a hard material used in the production of machining tools. Due to the existence of both tungsten carbide (WC) and cobalt (Co), WC-Co has the simultaneous features of hardness and toughness. After deposition of WC-Co, the part was machined to the shape of tools.

Results and Discussion

Microstructure Analysis of On-Fiber Thin Films. Figures 9 and 10 depict the microstructure of the samples at magnifications of 20 k× and 35 k× during laser sintering. As seen, at the laser power of 1.35 W, the nanoparticles have been slightly sintered, where neck-shape formation is rarely seen in this sample. As the laser power increases, the agglomeration and neck-shape formation are observed in the nanoparticles. At the maximum achievable power of 3.28 W, close-packed sintered particles are observed.

Crystal Structure of On-Fiber Thin Films. Figure 11 shows the XRD spectra of unsintered films and the films sintered at laser powers of 2.41 W and 3.28 W. The existence of multiple peaks in the XRD spectra implies that the silver nanoparticles are polycrystalline. The magnified image of the XRD peaks at 44° associated with (200) planes are also shown in Fig. 12. According to the magnified image, the peak of the untreated sample is broader than that of laser-sintered samples. The full-width-at-half-maximum (FWHM) of the unsintered sample, and the samples sintered at 2.41 W and 3.28 W are 0.77°, 0.65°, and 0.63°, respectively. The increase of the FWHM in the X-ray diffraction is related to the crystallite structure [33]. As the laser power increases, the particles agglomerate and the level of periodic arrangement in the crystals increases. This results in sharper peaks when the X-ray beam is diffracted.

Mechanical Properties of On-Fiber Thin Films. For the nanoindentation tests, six locations which were 10 μm apart were selected. A maximum load of 1000 μN was applied at each location, and the load-displacement curves were obtained. Figure 13 shows the indentation profiles of six locations in a sample taken by the nanoindenter tip.

Figure 14 shows the load-displacement curves for each sample at five indentation locations 2–6 labeled in Fig. 13. According to the Oliver–Pharr method [34], the indentation hardness (H) is obtained from

$$H = \frac{P_m}{A} \qquad (12)$$

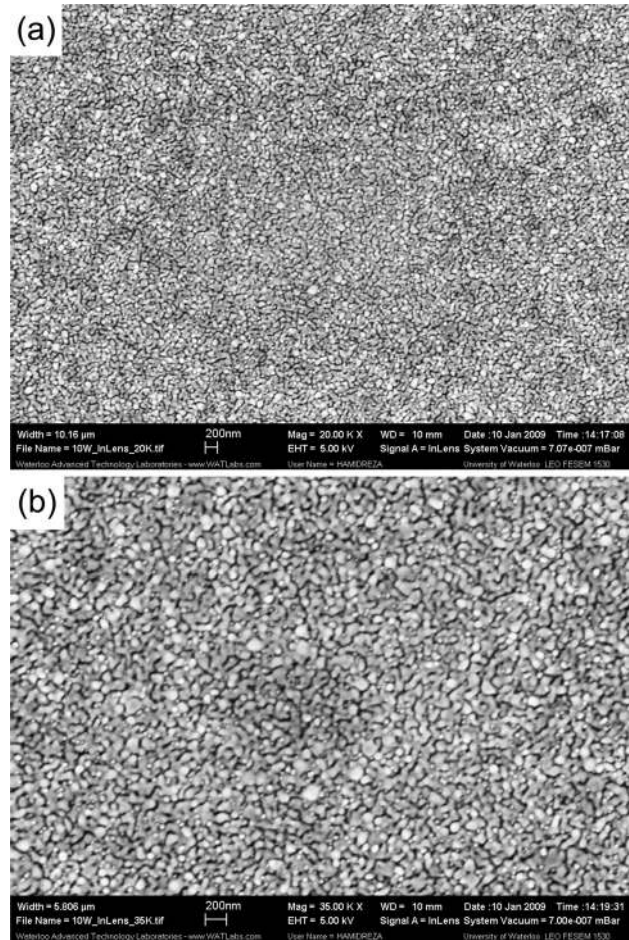where P_m is the maximum applied load, and A is the contact area between the indenter and the silver layer.
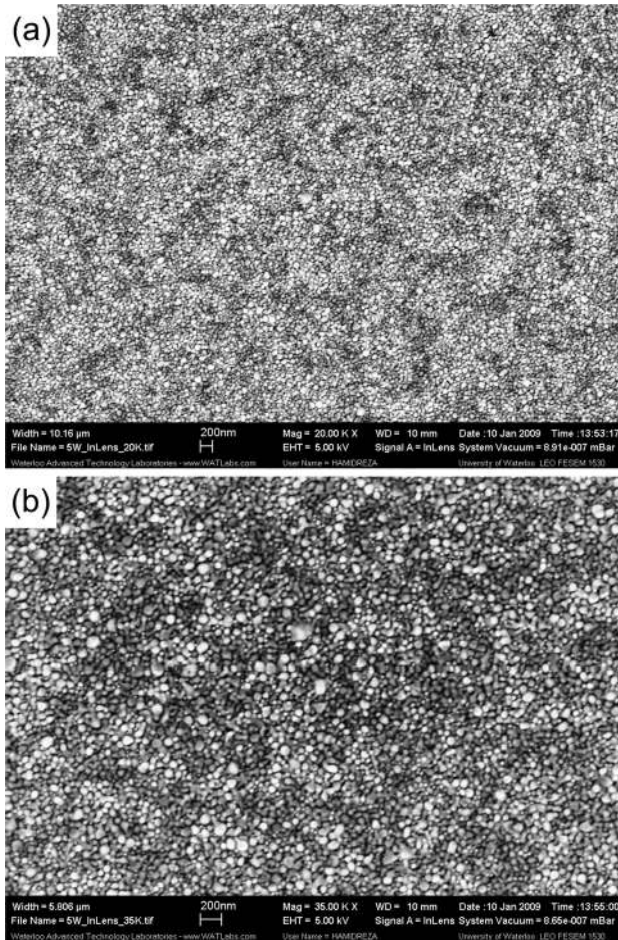
Fig. 9 In-lens images of the microstructure of the silver thin film sintered at 1.35 W taken at magnifications of (*a*) 20 k× and (*b*) 35 k×

Fig. 10 In-lens images of the microstructure of the silver thin film sintered at 3.28 W at magnifications of (*a*) 20 k× and (*b*) 35 k×

In addition, the nanoindentation test results were employed to obtain the modulus of elasticity of the deposited silver layers. The modulus of elasticity is related to the initial slope of the relaxation curve in the force-displacement graph as follows [35]:

$$S = \frac{2\alpha^* E^* A^{1/2}}{\sqrt{\pi}} \qquad (13)$$

where S is the initial slope of the relaxation curve, α^* is a correction factor for the shape of the indenter, and E^* is the reduced modulus of elasticity, which is related to the modulus of elasticity of the film and the indenter, as follows:

$$E^* = \left(\frac{1 - \nu_f^2}{E_f} + \frac{1 - \nu_{in}^2}{E_{in}} \right)^{-1} \qquad (14)$$
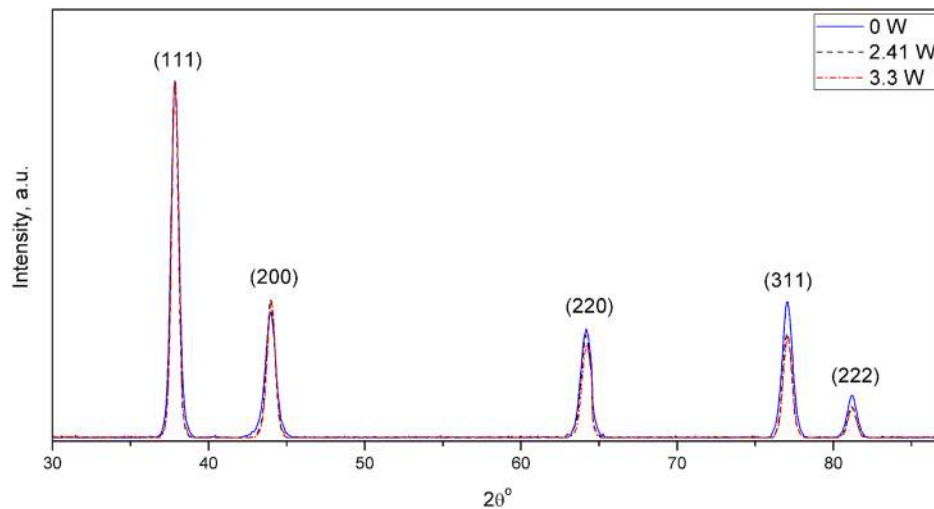
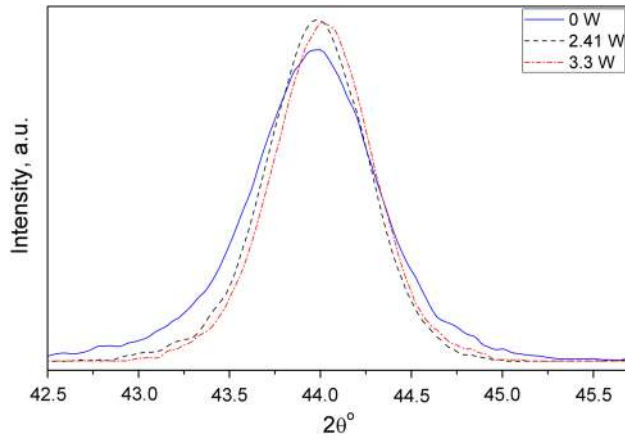**Fig. 11 XRD spectra of the silver thin films sintered at different laser powers**

Fig. 12 XRD peaks for (200) planes at different laser powers

ν is the Poisson's ratio, and subscripts *f* and *in* denote the film and the indenter properties. The modulus of elasticity of the deposited silver thin films can be obtained by using Eq. (13) and Eq. (14). The mechanical properties of the indenter are $E_{in} = 1140$ GPa and $\nu_{in} = 0.07$, and $\nu_f = 0.37$ is used for silver.

The hardness and modulus of elasticity, obtained from the nanoindentation test results, are plotted in Figs. 15 and 16. It is clear that hardness and modulus of elasticity increase by increasing the laser power. This is attributed to the agglomeration and sintering of nanoparticles. Close values of hardness have been reported for silver thin films [36,37]. In these experiments, the maximum obtained value for modulus of elasticity is 65 GPa, which is ~21% less than that of bulk silver (83 GPa). This may be caused by the differences in the samples microstructure, affected by the type of the fabrication process [36]. In addition, the agglomeration of the nanoparticles might not be complete and may contain porosity. The surface morphology such as the roughness of the deposited silver layers may also cause the discrepancies.

Microstructure Analysis of the Part with Embedded FBG. A prototyped sample with embedded FBG is shown in Fig. 17. The microscopic images of the cross section of the sample with embedded FBG are shown in Fig. 18. The optical fiber, the electroplated nickel layer, and the steel part are labeled in the figure. A magnified image of the optical fiber, the silver thin film with a thickness of 1.7–2.3 μm, and the electroplated nickel layer
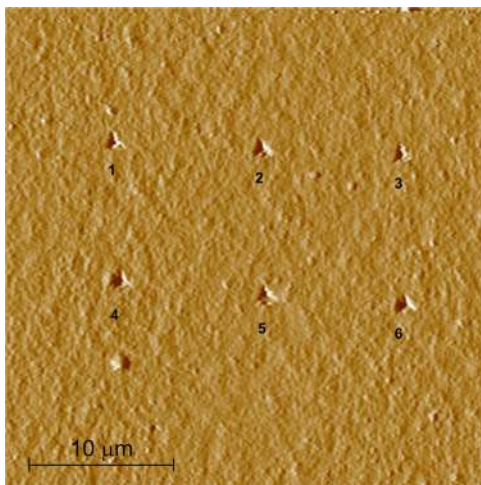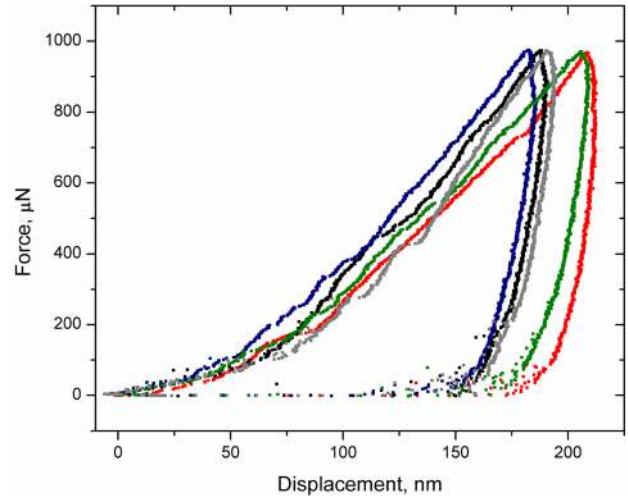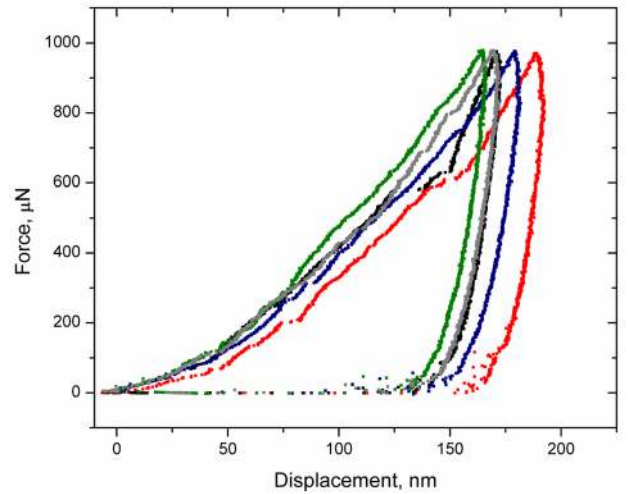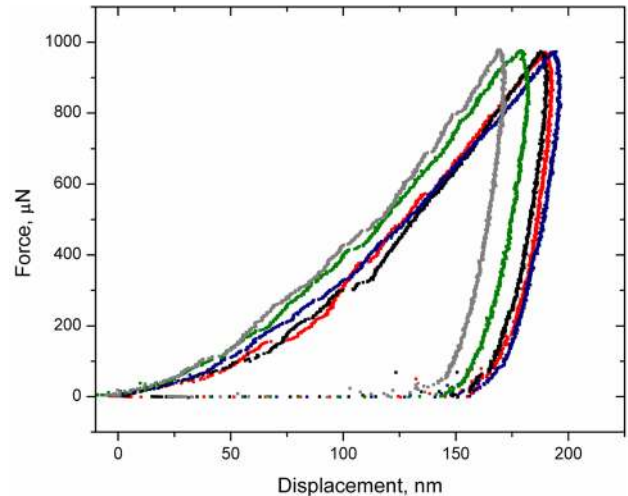

Fig. 13 Nanoindentation profiles at six locations on a silver thin film

(a)

(b)

(c)

Fig. 14 Load displacement curves obtained from the nanoindentation test at five locations of the silver thin films sintered at (*a*) 1.35 W, (*b*) 2.41 W, and (*c*) 3.28 W

are also depicted. According to the figure, there is a crack free interface between the optical fiber and the silver layer as well as the silver and nickel layers. The black spots in the figure are the residues of materials used for polishing the cross section.
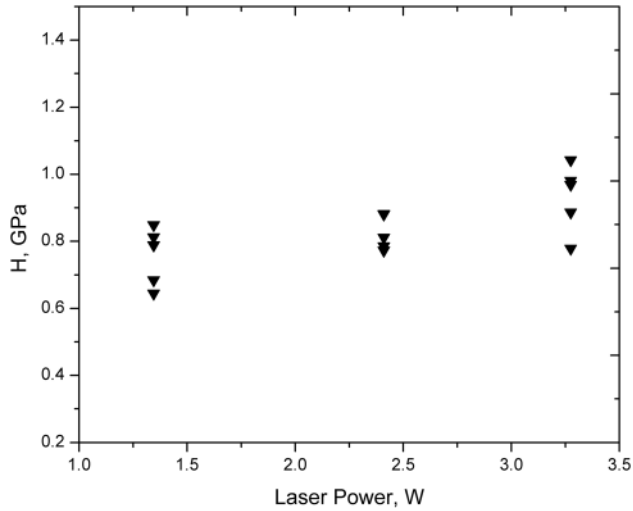
Fig. 15   Hardness of silver thin films as a function of incident laser power obtained from nanoindentation tests
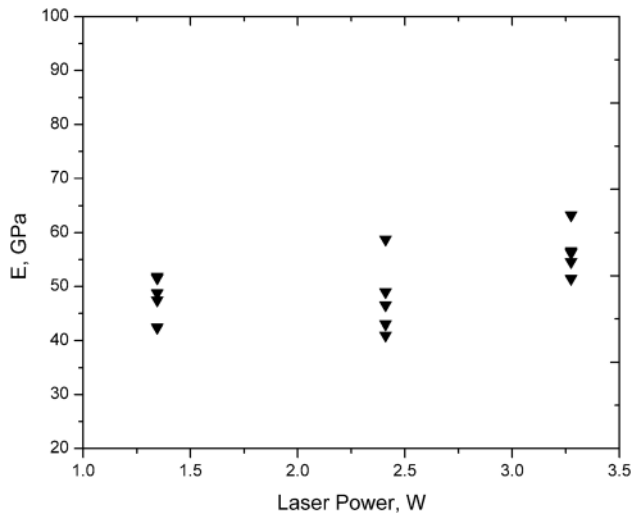

Fig. 16   Modulus of elasticity of silver thin films as a function of incident laser power obtained from nanoindentation tests

Sensitivity Analysis. The reflection spectra of the FBG before and after the embedding process are plotted in Fig. 19. As seen, the two graphs are only slightly different implying that the magnitudes of residual stresses generated during the embedding process
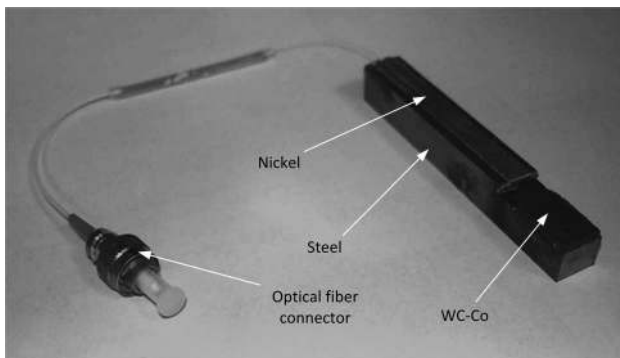

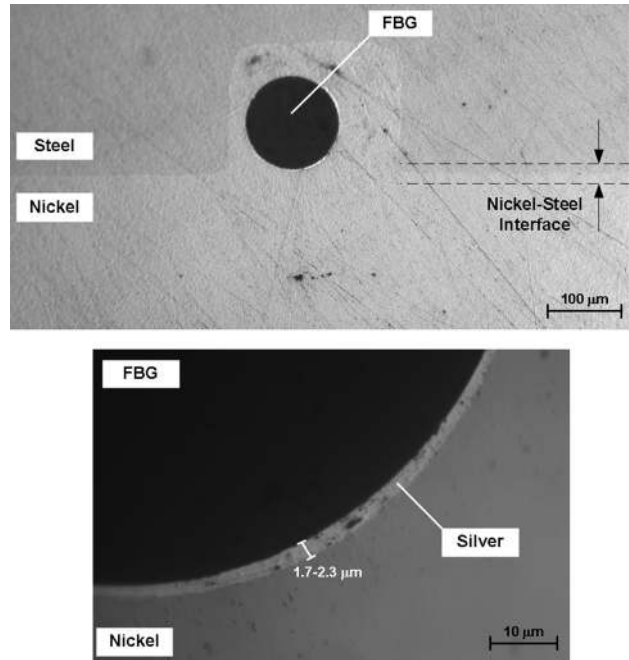**Fig. 17   Prototyped sample with metal-embedded FBG using LAMM and electroplating**

Fig. 18   Cross section of the sample with embedded FBG manufactured by LAMM and nickel electroplating

are very small. According to the figure, the FWHM of the Bragg peak is reduced from 0.321 nm to 0.272 nm. This is related to the compressive stress generated on the optical fiber during the electroplating process. According to Ref. [1], the normalized bandwidth of Bragg gratings at the band edges is obtained from $\Lambda\lambda/\lambda = \nu_f \overline{\Delta n}/n_{\mathrm{eff}}$, where ν_f and $\overline{\Delta n}$ are the properties of the grating. Compressive strain increases the index of refraction n_{eff} (according to Eq. (2)), which leads to the reduction of the bandwidth.

To investigate the performance of the embedded sensor, the prototyped sample was tested through a heating process on a hot plate, which simultaneously applied temperature and strain on the embedded FBG. The reflection spectra of the FBG were obtained at different temperatures. Figure 20 gives the reflection spectra at different temperatures ranging from 32.2 to 121.7 °C. The variations of the Bragg wavelength as a function of temperature are shown in Fig. 21. The thermal process not only increases the FBG's temperature but also induces strain in the optical fiber,
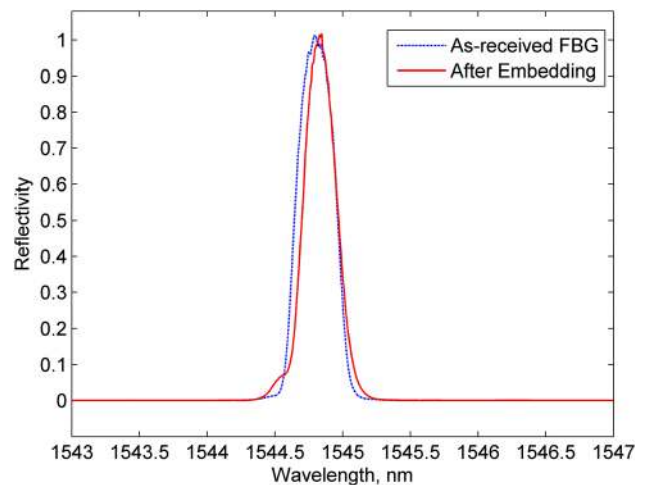

Fig. 19   Reflection spectra of the FBG before and after embedding at room temperature
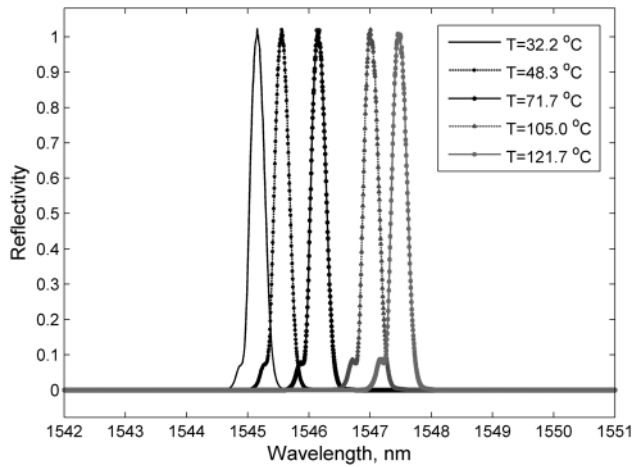
Fig. 20 Reflection spectra of the embedded FBG at different temperatures ranging from 32.2 to 121.7 °C

Fig. 21 Bragg wavelength as a function of temperature obtained from experiments for embedded FBG showing a sensitivity of 25.8 pm/°C
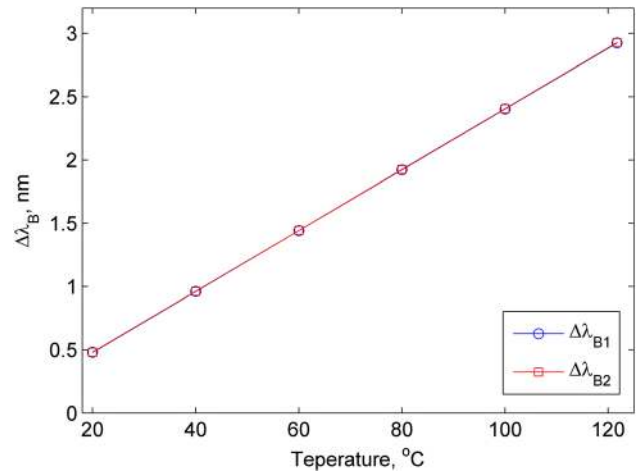

Fig. 22 Bragg wavelength changes of the embedded FBG as a function of temperature obtained from optomechanical modeling showing a sensitivity of 24 pm/°C
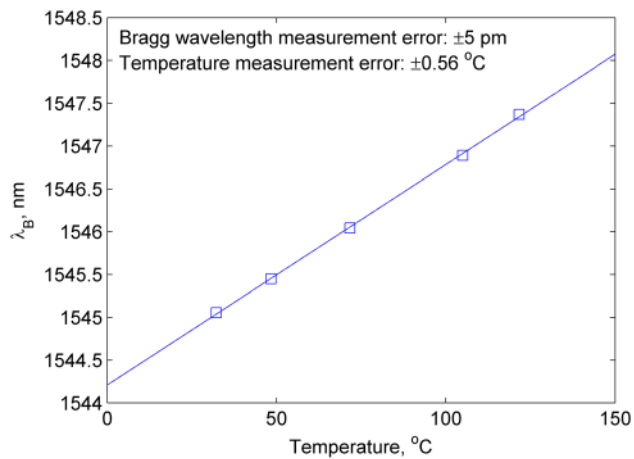
revealed in the microscopic images. The linear trend also shows that the materials, especially the silver thin film, are in the elastic region and the generated thermal stress has not exceeded their yield strength.

The temperature sensitivity obtained from this graph is 25.8 pm/°C, which is around 2.58 times larger than that of a bare FBG (~10 pm/°C). This is attributed to the large coefficient of thermal expansion of the metal part, which is $13.4 \times 10^{-6} \, °C^{-1}$ for nickel and $11.8 \times 10^{-6} \, °C^{-1}$ for steel-1.

The developed optomechanical model was run to investigate the sensitivity of the embedded FBG. The modeling results showing Bragg wavelength shift as a function of temperature are plotted in Fig. 22. The graphs are plotted for $\Delta\lambda_{B1}$ and $\Delta\lambda_{B2}$ obtained from Eq. (7). The difference between $\Delta\lambda_{B1}$ and $\Delta\lambda_{B2}$ can hardly be detected meaning the transverse strain components are very close. According to the graph, the thermal sensitivity is 24 pm/°C indicating a difference of about 7.5%.

The achieved sensitivity in this experiment is higher compared to the embedded FBG reported in Ref. [7] with a sensitivity of 21 pm/°C. This is attributed to the differences in the geometrical dimensions.

Figure 23 shows the von Mises stress obtained from the FE modeling at a temperature of 121.7°C. The maximum von Mises stress in the optical fiber corresponding to the temperature of

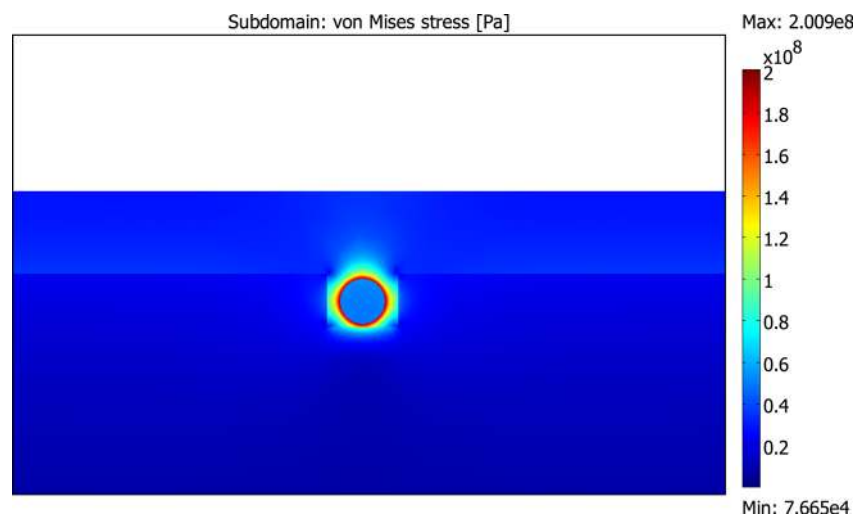which concurrently affect the reflection spectrum of FBG. According to Fig. 21, the sensor preserves its linear behavior implying a good integrity between the layers, which was also

Fig. 23 FE analysis results for von Mises stress at 121.7 °C

121.7°C is obtained from the FE model and is equal to 53.5 MPa, which is far below the damage threshold of the optical fiber. Accordingly, the maximum von Mises stress occurs in the silver thin film and is equal to 200 MPa. The linear response of the optical fiber proves that the stress in the silver thin film has not caused the silver layer to pass the elastic region.

Conclusions

A low temperature technique consisting of silver thin film deposition using LAMM and electroplating was employed in this research work for embedding FBGs in metal structures. To realize the application of embedded FBG sensors in structural analysis of machining tools, the electroplating process was followed by the deposition of WC-Co using LSFF.

The LAMM process was characterized to study the effects of process parameters, specifically the laser sintering parameters, on the microstructure, crystal structure, and mechanical properties of the thin films. The characterization scheme showed that laser power has a prominent effect on the properties of the silver thin films including the agglomeration of particles, crystalline structure distinguished by sharpening of the XRD peaks, and the mechanical properties (e.g., modulus of elasticity and hardness). The results of the thermal cycle test of the embedded sensor showed a linear trend in the response, which was in agreement with the modeling results derived from the optomechanical model developed based on the photo-elastic and thermo-optic properties of FBGs. The linear response of the embedded sensor indicates the integrity of the layers and the absence of cracks, porosity, and delamination which was also confirmed by microscopic imaging.

As future work, the authors will pursue the design, manufacturing, and testing of machining tools with embedded FBG sensors including the positioning of the sensors for optimal performance.

References

[1] Erdogan, T., 1997, "Fiber Grating Spectra," J. Lightwave Technol., **15**(8), pp. 1277–1294.
[2] Kashyap, R., 2010, Fiber Bragg Gratings, 2nd ed., Academic Press, Burlington, MA.
[3] "Corning SMF-28 Optical Fiber Product Information," Corning Inc., Corning, NY, 2002.
[4] Guemes, J. A., and Menendez, J. M., 2002, "Response of Bragg Grating Fiber-Optic Sensors When Embedded in Composite Laminates," Compos. Sci. Technol., **62**, pp. 959–966.
[5] Lau, K. T., Chanb, C. C., Zhoua, L. M., and Jin, W., 2001, "Strain Monitoring in Composite-Strengthened Concrete Structures Using Optical Fibre Sensors," Composites, Part B, **32**, pp. 33–45.
[6] Kuang, K. S. C., and Cantwell, W. J., 2003, "Use of Conventional Optical Fibers and Fiber Bragg Gratings for Damage Detection in Advanced Composite Structures: A Review," Appl. Mech. Rev., **56**(5), pp. 493–513.
[7] Li, X. C., Prinz. F., and Seim, J., 2001, "Thermal Behavior of A Metal Embedded Fiber Bragg Grating Sensor," Smart Mater. Struct., **10**, pp. 575–579.
[8] Cheng, X., Datta, A., Choi, H., Zhang, X., and Li, X., 2007, "Study on Embedding and Integration of Microsensors into Metal Structures for Manufacturing Applications," ASME J. Manuf. Sci. Eng., **129**, pp. 416–424.
[9] Zhang, X., Choi, H., Datta, A., and Li, X., 2006, "Design, Fabrication, and Characterization of Metal Embedded Thin Film Thermocouples With Various Film Thicknesses and Junction Size," J. Micromech. Microeng., **16**, pp. 900–905.
[10] Shen, Y., He, J., Qiu, Y., Zhao, W., Chen, S., Sun, T., and Grattan, K. T. V., 2007, "Thermal Decay Characteristics of Strong Fiber Bragg Gratings Showing High-Temperature Sustainability," J. Opt. Soc. Am. B, **24**(3), pp. 430–438.
[11] Bucaro, J. a., and Dardy, H. D., 1974, "High-Temperature Brillouin Scattering in Fused Quartz," J. Appl. Phys., **45**(12), pp. 5324–5329.
[12] Lee, C. E., Gibler, W. N., Atkins, R. A., Alcoz, J. J., and Taylor, H. F., 1991, "Metal-Embedded Fiber-Optic Fabry-Perot Sensors," Opt. Lett., **16**, pp. 1990–1992.
[13] Sandlin, S., Kinnunen, T., Ramo, J., and Sillanpaa, M., 2006, "A Simple Method For Metal Re-Coating of Optical Fibre Bragg Gratings," Surf. Coat. Technol., **201**, pp. 3061–3065.
[14] Kong, C. Y., and Soar, R., 2005, "Methods for Embedding Optical Fibers in an Aluminum Matrix by Ultrasonic Consolidation," Appl. Opt., **44**, pp. 6325–6333.
[15] Lupi, C., Felli, F., Ippoliti, L., Caponero, M. A., Ciotti, M., Nardelli, V., and Paolozzi, A., 2005, "Metal Coating for Enhancing the Sensitivity of Fibre Bragg Grating Sensors at Cryogenic Temperature," Smart Mater. Struct., **14**, pp. N71–N76.
[16] Li, L., Geng, R., Zhao, L., Chen, G., Chen, G., Fang, Z., and Lam, C., 2003, "Response Characteristics of Thin-Film-Heated Tunable Fiber Bragg Gratings," IEEE Photonics Technol. Lett., **15**(4), pp. 545–547.
[17] Steinvurzel, P., MacHarrie, R., Baldwin, K., Van Hise, C., Eggleton, B., and Rogers, J., 2005, "Optimized of Distributed Resistive Metal Film Heaters in Thermally Tunable Dispersion Compensators for High-Bit-Rate Communication Systems," Appl. Opt., **44**(14), pp. 2782–2791.
[18] Fox, G., Muller, C., Setter, N., Costantini, D., Ky, N., and Limberger, H., 1997, "Wavelength Tunable Fiber Bragg Grating Devices Based on Sputter Deposited Resistive and Piezoelectric Coatings," J. Vac. Sci. Technol. A, **15**(3), pp. 1791–1795.
[19] Sutapun, B., Tabib-Azar, M., and Kazemi, A., 1999, "Pd-Coated Elastooptic Fiber Optic Bragg Grating Sensors for Multiplexed Hydrogen Sensing," Sens. Actuators B, **60**(1), pp. 27–34.
[20] Alemohammad, H., and Toyserkani, E, "Smart Tools with Embedded Optical Fibers: Laser Based Layered Manufacturing Procedures," Proceedings of ICALEO 2009, **102**, pp. 1160–1164.
[21] Othonos, A. and Kalli, K., 1999, Fiber Bragg Gratings, 1st ed., Artech House, Boston.
[22] Buck, J. A., 2004, Fundamentals of Optical Fibers, 2nd ed., Wiley, Hoboken.
[23] Alemohammad, H., 2010, "Development of Optical Fiber-Based Sensing Devices Using Laser Microfabrication Methods," Ph.D. thesis, University of Waterloo, Waterloo, Canada.
[24] Kim, K. S., Kollar, L., and Springer, G.S., 1993, "A Model of Embedded Fiber Optic Fabry–Perot Temperature and Strain Sensors," J. Compos. Mater., **27**, pp. 1618–1662.
[25] Alemohammad, H., Toyserkani, E., 2009, "Simultaneous Measurement of Temperature and Tensile Loading using Tunable Superstructure FBGs Developed by Laser-Direct Writing of Periodic On-Fiber Metallic Films," Smart Mater. Struct., **18**(9), article no. 095048.
[26] Alemohammad, H., Aminfar, O., and Toyserkani, E., 2008, "Morphology and Microstructure Analysis of Nano-Silver Thin Films Deposited by Laser-Assisted Maskless Microdeposition," J. Micromech. Microeng., **18**(11), article no. 115015.
[27] Piqué, A., Chrisey, D. B., Auyeung, R. C. Y., Fitz-Gerald, J., Wu, H. D., McGill, R. A., Lakeou, S., Wu, P. K., Nguyen, V., and Duigna, M., 1999, "A Novel Laser Transfer Process for Direct Writing of Electronic and Sensor Materials," Appl. Phys. A, **69**, pp. S279–S284.
[28] Nakaso, K., Shimada, M., Okuyama, K., and Deppert, K., 2002, "Evaluation of The Change in The Morphology of Gold Nanoparticles During Sintering," J. Aerosol Sci., **33**(7), pp. 1061–1074.
[29] Auyeung, R. C. Y., Kim, H., Mathews, S. A., and Piqué, A., 2007, "Laser Direct-Write of Metallic Nanoparticle Inks," J. Laser Micro/Nanoeng., **2**(21), pp. 21–25.
[30] Arcidiacono, S., Bieri, N. R., Poulikakos, D., and Grigoropoulos, C. P., 2004, "On the Coalescence of Gold Nanoparticles," Int. J. Multiphase Flow, **30**(7–8), pp. 979–994.
[31] Greer, J., and Street, R., 2007, "Thermal Cure Effects on Electrical Performance of Nanoparticle Silver Inks," Acta Mater., **55**(18), pp. 6345–6349.
[32] Paul, C. P., Alemohammad, H., Toyserkani, E., Khajepour, A., and Corbin, S., 2007, "Cladding of WC-12Co on Low Carbon Steel Using a Pulsed Nd: YAG Laser," Mater. Sci. Eng., A, **464**(1–2), pp. 170–176.
[33] Moon, K. S., Dong, H., Maric, R., Pothukuchi, S., Hunt, A., Li, Y., and Wong, C. P., 2005, "Thermal Behavior of Silver Nanoparticles for Low-Temperature Interconnect Applications," J. Electron. Mater., **34**(2), pp. 168–175.
[34] Oliver, W. C., and Pharr, G. M., 1992, "An Improved Technique for Determining Hardness and Elastic Modulus Using Load and Displacement Sensing Indentation Experiments," J. Mater. Res., **7**(6), pp. 1564–1583.
[35] Freud, L. B. and Suresh, S., 2003, Thin Film Materials, Cambridge University, Cambridge, UK, p. 545.
[36] Cao, Y., Allameh, S., Nankivil, D., Sethiaraj, S., Otiti, T. and Soboyejo, W., 2006, "Nanoindentation Measurements of the Mechanical Properties of Polycrystalline Au and Ag Thin Films on Silicon Substrates: Effects of Grain Size and Film Thickness," Mater. Sci. Eng. A, **427**(1–2), pp. 232–240.
[37] Panin, A., Shugurov, A. and Oskomov, K., 2005, "Mechanical Properties of Thin Ag Films on a Silicon Substrate Studied Using the Nanoindentation Technique," Phys. Solid State, **47**(11), pp. 2055–2059.